Biomedical Signal Processing and Control 129 (2027) 111350

Contents lists available at ScienceDirect

Biomedical Signal Processing and Control

journal homepage: www.elsevier.com/locate/bspc

Robust differential spiral EIS co-design for bladder cancer urine sensing with measured-data validation

Mohanad A. Deif [a,b], Ismail A. Elhaty [c], Mohamed A. Hafez [d,e], Mohammad Khishe [f,*]

[a] Research Institute of Sciences and Engineering, University of Sharjah, Sharjah, United Arab Emirates
[b] Department of Computer Science, College of Information Technology, Misr University for Science and Technology (MUST), Giza, Egypt
[c] Department of Nutrition and Dietetics, Faculty of Health Sciences, Istanbul Gelisim University, Istanbul, Turkey
[d] Faculty of Engineering, INTI International University, Nilai, Malaysia
[e] Shinawatra University, Bangkok, Thailand
[f] Applied Science Research Center, Applied Science Private University, Amman, Jordan

ARTICLE INFO

Dataset link: http://dx.doi.org/10.1038/s41598-019-42776-9

Keywords:
Electrical impedance spectroscopy (EIS)
Differential sensing
Spiral biosensor
Robust co-design
Fisher information
Parameter identifiability
Urine sensing
Bladder cancer surveillance prescreening

ABSTRACT

This paper presents a robust co-design framework for differential spiral electrical impedance spectroscopy (EIS) biosensors, developed as an in silico methodological study for urine-sensing applications in bladder cancer surveillance. The objective is to improve parameter identifiability in label-free differential urine sensing when nuisance effects, fabrication tolerances, and reference mismatch reduce estimation reliability. The framework combines differential sensing to suppress shared common-mode nuisance with joint optimization of sensor geometry and frequency selection. The design is formulated as a minimax Fisher-information problem to improve worst-case identifiability.

The primary co-design evaluation uses an application-motivated synthetic protocol with matched budgets and multiple baselines. The proposed method improves worst-case identifiability and Cramér–Rao lower-bound proxy metrics at the same frequency budget, with consistent gains under budget variation, uncertainty amplification, and reference mismatch. To examine transfer beyond the synthetic model family at component level, we additionally analyzed an independent measured EIS dataset using grouped hold-out validation and training-only empirical minimax frequency selection. At a four-frequency budget, the measured-data analysis achieved a balanced accuracy of $79.6\% \pm 11.6\%$, compared with $70.4\% \pm 14.0\%$ for log-uniform selection and $74.1\% \pm 8.5\%$ for the full 101-frequency spectrum. This independent analysis supports the differential sparse-frequency design principle outside the synthetic generator, but it does not validate the optimized spiral geometry, urine sensing, bladder-cancer diagnosis, or clinical readiness.

1. Introduction

Electrical impedance spectroscopy (EIS) is a widely used method for measuring frequency-dependent electrical behavior in electrochemical and biosensing systems. It is attractive because a single frequency sweep can capture information about material, interface, and transport processes across multiple scales [1–4]. In label-free biosensing, EIS is also appealing because it can support direct sensing without chemical labels and can be implemented with compact and relatively low-cost hardware [5–7].

In this work, we study the methodology in an application-motivated setting related to urine sensing for bladder cancer surveillance. This context is clinically relevant because bladder cancer follow-up often involves repeated surveillance, and urine-based tests are of continuing interest as supportive tools within surveillance workflows. At the same time, current guidelines emphasize that urinary markers should not replace cystoscopic evaluation [8,9]. Accordingly, the present study does not claim clinical validation or diagnostic readiness. Instead, it uses this medical context to motivate a robust in silico design framework for future adjunct urine-sensing systems.

Reliable parameter estimation from EIS data remains difficult in practice. Real measurements can be affected by nuisance signals, fabrication tolerances, drift, and reference mismatch, and these effects can reduce identifiability even when nominal sensitivity appears strong. As a result, a design that performs well under idealized conditions may become unstable under uncertainty, which limits practical deployment in biosensing applications [10,11].

A second challenge is that key design choices are often handled separately. The sensing operator, sensor geometry, and frequency set

* Corresponding author at: Applied Science Research Center, Applied Science Private University, Amman, Jordan.
E-mail address: m_khishe@alumni.iust.ac.ir (M. Khishe).

https://doi.org/10.1016/j.bspc.2026.111350
Received 1 March 2026; Received in revised form 16 July 2026; Accepted 18 August 2026
Available online 27 August 2026

Table 1
Summary of related work and the gap addressed in this study.

Reference(s)	Area	Main contribution	Limitation relative to this work
[1–5]	EIS foundations and tutorials	Establish EIS theory, measurement workflow, and interpretation principles across applications.	Do not address differential spiral co-design or robust minimax identifiability optimization.
[6,7,10,11]	Label-free impedance biosensing	Show the value of impedimetric biosensing and discuss practical limits in reproducibility and reliability.	Do not formulate estimation-driven co-design under uncertainty.
[12]	Geometry optimization	Demonstrates that electrode geometry strongly affects sensitivity and detection performance.	Focuses on nominal sensitivity, not joint geometry and frequency optimization for worst-case identifiability.
[13–15]	Multichannel and differential sensing hardware	Shows multichannel and differential readout methods that improve common-mode rejection and small-signal detection.	Provides hardware motivation, but not uncertainty-aware co-design of geometry and frequency selection.
[23]	Identifiability in impedance models	Clarifies identifiability conditions in impedance modeling and the role of model structure.	Does not address robust sensor and experiment co-design for practical worst-case identifiability.
[19,20,24]	Classical optimal experimental design	Provides mathematical foundations for informative experiment design and optimality criteria.	General framework only; not specialized to differential spiral EIS biosensors.
[18,25,26]	Estimation and system identification	Establishes FIM/CRLB reasoning and the effect of excitation design on estimation quality.	Foundational only; not integrated with sensor architecture co-design.
[21,22]	Modern and robust OED	Extends OED to modern computation and uncertainty-aware min–max formulations.	Not directly linked to differential EIS biosensor geometry and frequency co-design.
This work	Differential EIS robust co-design	Combines differential sensing, geometry optimization, and frequency selection in a minimax Fisher-information framework for worst-case identifiability under synthetic uncertainty.	The geometry co-design evidence remains synthetic; the added measured-data analysis validates only the differential sparse-frequency component.

are commonly selected one at a time or by heuristic rules, even though they are strongly coupled in EIS and jointly determine sensitivity and estimation uncertainty. Consequently, improving only one part of the system does not necessarily improve overall identifiability [12–15]. Related biosensor studies in adjacent sensing modalities also show that architecture design, material configuration, and frequency-selective behavior can strongly influence sensing performance, as seen in recent nanophotonic and metasurface-based sensor platforms [16,17].

This study addresses this gap by proposing a robust co-design framework for differential spiral EIS biosensing under synthetic uncertainty. The method combines a differential sensing operator, intended to suppress shared common-mode nuisance, with joint optimization of sensor geometry and frequency selection. The design is formulated as a minimax problem based on Fisher information so that the objective targets worst-case identifiability rather than nominal performance alone [18–22].

We evaluate the main co-design framework using an application-motivated synthetic protocol with matched budgets and multiple baselines, including single-channel, differential-only, and partial co-design variants. The results and ablation analyses show improved worst-case identifiability and measurement efficiency under the stated synthetic uncertainty model. We also add a component-level analysis on independently measured EIS spectra to test whether differential sparse-frequency interrogation remains informative outside the synthetic generator. The study should still be interpreted as a methodological contribution rather than confirmation of a fabricated urine sensor or a clinically deployable biosensor [23–25].

2. Related work

Electrochemical impedance spectroscopy (EIS) is a mature method for studying frequency-dependent electrical behavior in electrochemical and biosensing systems. Foundational books and modern reviews explain the main theory, measurement workflow, and common applications, and they also show that interpretation quality depends on modeling assumptions, excitation design, and noise handling [1–5]. This makes EIS informative, but it also makes reliable parameter estimation difficult when uncertainty is present.

In label-free biosensing, impedance methods remain attractive because they support direct sensing, compact instrumentation, and relatively low-cost integration. At the same time, many reviews report practical limitations such as nonspecific effects, interface variability, and environmental changes, which can reduce reproducibility and estimation reliability [6,7,10,11]. These studies motivate better biosensor architecture and measurement strategy, but they do not formulate design as a worst-case identifiability optimization problem. Recent non-EIS biosensor studies also highlight the importance of deliberate platform design, including graphene-enhanced terahertz metasurface SPR architectures for cancer-oriented detection and multilayer SPR biosensors for ultrasensitive biomarker sensing [27,28].

Another important line of work focuses on sensor geometry. Recent finite-element studies show that parameters such as electrode gap, width, and height strongly affect sensitivity and detection performance [12]. This confirms that geometry is a major design variable, but most geometry studies optimize nominal sensitivity or task-level performance and do not jointly optimize geometry and the frequency set using an estimation-theoretic objective.

Differential and multichannel impedance sensing is also well motivated in the hardware literature. Multichannel analyzers and differential readout circuits can reduce common disturbances and improve detection of small changes, while also revealing practical limitations such as mismatch and common-mode leakage [13–15]. These studies support differential sensing, but they do not provide a unified framework that jointly optimizes sensor geometry and measurement frequencies under uncertainty.

The mathematical basis for principled measurement selection comes from optimal experimental design, Fisher information analysis, and identifiability theory. Classical references provide the foundations of optimality criteria and Cramér–Rao-based reasoning, and system identification texts explain how experiment design affects estimation quality [18–20,24–26]. Modern surveys extend these ideas to more complex settings [21], and identifiability work in impedance modeling shows

that practical identifiability depends on excitation and data conditions, not only on model structure [23]. Robust experiment design also addresses uncertainty explicitly through min–max formulations [22].

The main gap is the lack of a single framework that combines differential sensing, geometry optimization, and frequency selection under uncertainty with a minimax identifiability objective. This gap is important for application-motivated biosensor development, including urine-based bladder cancer surveillance prescreening, where robustness and measurement consistency are essential for future adjunct workflows [8,9]. The present work addresses this gap by combining a differential sensing operator with joint geometry and frequency co-design in a robust Fisher-information-based framework. Table 1 summarizes the main lines of previous work and clarifies the position of this study.

3. Problem statement and main study contribution

Electrical impedance spectroscopy (EIS) is useful for label-free biosensing, but reliable parameter estimation is often difficult in practice. Real measurements are affected by nuisance signals, fabrication tolerances, drift, and reference mismatch. These effects can reduce identifiability even when nominal sensitivity looks strong.

This issue is important in urine-sensing applications related to bladder cancer surveillance, where future practical translation would depend on stable and repeatable measurements. In this study, the goal is not clinical diagnosis. The goal is to support robust urine biofluid sensing under uncertainty in an application-motivated in silico setting.

Another challenge is that key design choices are often made separately. The sensing operator, sensor geometry, and interrogation frequencies are usually selected one by one or by heuristics. In EIS, however, these choices are coupled because they jointly affect sensitivity and estimation uncertainty. This can lead to suboptimal performance, especially when the frequency budget is limited.

The main problem in this work is how to design a differential spiral EIS biosensing system that remains identifiable under uncertainty while using a limited number of frequencies. The focus is on improving worst-case identifiability, not only nominal performance.

Fig. 1 summarizes the study. Panel (a) shows the differential spiral sensing concept with a urine sample and a reference urine matrix, using $\Delta Z = Z_s - Z_r$ to reduce shared nuisance effects. Panel (b) shows the simplified readout and acquisition chain. Panel (c) shows the co-design outcome, where geometry and a frequency subset are selected to improve robust identifiability.

To address this problem, we propose a robust co-design framework for differential spiral EIS biosensing under synthetic uncertainty. The framework combines a differential sensing operator with joint optimization of sensor geometry and frequency selection. The design uses a Fisher-information-based minimax objective to improve worst-case identifiability.

The main contribution is a unified methodological and robust design framework that links differential sensing, geometry design, and frequency selection in one formulation. The study also provides a clear evaluation protocol with matched-budget comparisons and ablation analyses to show the value of each component.

The geometry co-design evaluation remains synthetic and model-dependent. An additional independent measured-data analysis tests the differential sparse-frequency principle outside the synthetic model family, but the study does not claim fabricated-sensor verification, urine-specific validation, or clinical readiness. Its contribution is a clear design strategy for subsequent hardware and biosample studies in urine-sensing applications related to bladder cancer surveillance.

4. Methodology

4.1. Preliminaries and notation

We formulate this study as a robust inverse-design problem for a differential spiral label-free EIS biosensor under dispersive uncertainty. The methodology is purely mathematical and is intentionally separated from fabrication, instrumentation, and clinical validation. In this work, the medical context is urine sensing in applications related to bladder cancer surveillance, but the present section remains a non-clinical, application-motivated in silico mathematical framework rather than an experimental or clinical study.

This section defines the differential sensor operator, the geometry–frequency co-design problem, and the synthetic uncertainty model used for methodological concept validation.

Let $\Omega \subset \mathbb{R}^3$ denote the sensing domain occupied by the interrogated medium. For angular frequency $\omega \in [\omega_{\min}, \omega_{\max}]$, the medium is represented by a complex admittivity field

$$\gamma(x, \omega; \theta) = \sigma(x; \theta) + j\omega\varepsilon(x; \theta), \qquad x \in \Omega, \tag{4.1}$$

where σ and ε denote conductivity and permittivity, respectively, and $\theta \in \Theta \subset \mathbb{R}^p$ is a latent parameter vector describing an effective dispersive biofluid state.

The sensor is parameterized by a geometry-design vector

$$d = \left(N, w, s, D_{\text{out}}, t_{\text{sub}}, \varepsilon_{\text{sub}}, g, w_g\right) \in \mathcal{D}, \tag{4.2}$$

where N is the number of turns, w is the trace width, s is the inter-trace spacing, D_{out} is the outer diameter, t_{sub} is the substrate thickness, ε_{sub} is the substrate relative permittivity, and (g, w_g) denote optional guard-gap and guard-width parameters used to shape fringing fields and stabilize differential coupling. The admissible set $\mathcal{D}$ encodes fabrication, symmetry, and packaging constraints.

The frequency-design variable is a cardinality-constrained subset

$$F = \{\omega_k\}_{k=1}^{m} \subset [\omega_{\min}, \omega_{\max}], \qquad |F| = m, \tag{4.3}$$

where m is a prescribed frequency budget reflecting measurement-time and electronics constraints.

Throughout, bold symbols denote finite-dimensional vectors, and $\succeq$ denotes positive semidefinite (PSD) matrix ordering.

4.2. Assumptions

The following assumptions are introduced only where mathematically needed and are consistent with the intended differential sensor architecture.

Assumption 1 (*Matched Differential Channels and Common-Mode Nuisance*)**.** The sensing and reference spiral channels are routed and interrogated through a nominally matched readout chain such that dominant nuisance effects (lead parasitics, stray coupling, environmental drift, front-end offsets) appear as a common-mode term depending on (d, ω), up to residual mismatch absorbed in the differential noise covariance. This assumption is introduced as an idealized modeling condition for the proposed differential architecture and does not imply perfect cancellation in practical fabricated systems, where additional channel mismatch and unmodeled non-idealities may remain.

Assumption 2 (*Known Reference Branch Response*)**.** The reference channel interacts with a fixed, known reference condition parameterized by θ_r (e.g., a reference urine matrix or a known reference stack response), and θ_r is treated as known in the forward model.

Assumption 3 (*Differentiability*)**.** The differential mean response is continuously differentiable with respect to θ and piecewise continuously differentiable with respect to the continuous components of d over the feasible region $\mathcal{D}$.

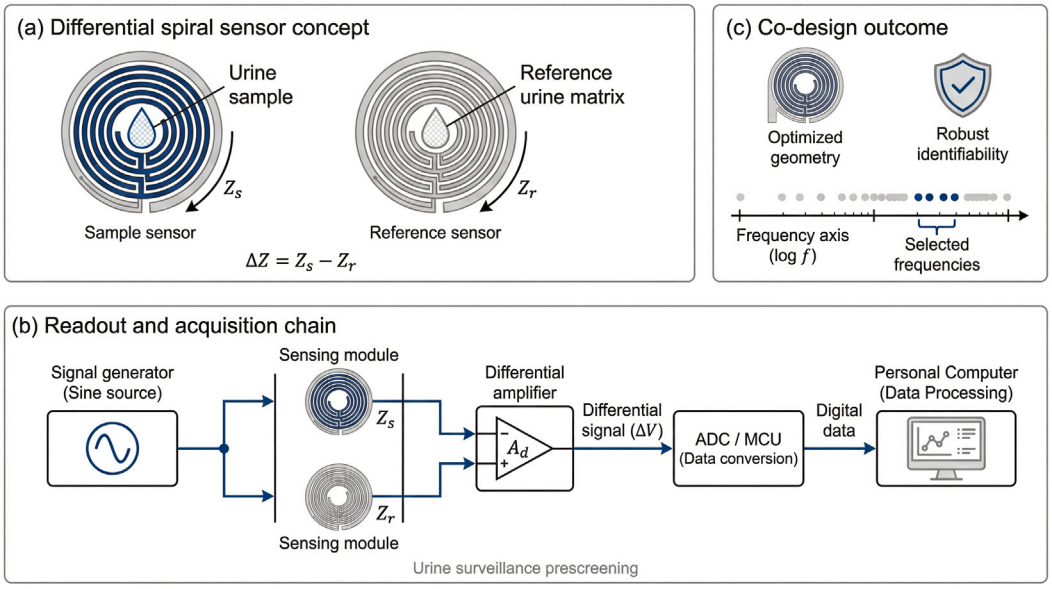

Fig. 1. Schematic overview of the proposed differential spiral EIS biosensing platform and the main study contribution for urine-sensing applications related to bladder cancer surveillance. (a) Differential spiral sensing concept with paired sample and reference sensors, where the differential response ($\Delta Z = Z_s - Z_r$) suppresses shared nuisance effects. (b) Simplified readout and acquisition chain with a single sine excitation source, sensing module, differential amplifier, ADC/MCU, and data processing. (c) Compact co-design outcome showing optimized geometry, selected frequencies on a one-dimensional frequency axis, and robust identifiability under uncertainty.

Assumption 4 (*Nondegenerate Residual Noise*)**.** For every feasible (d, F), the residual differential observation covariance $\Sigma(d, F)$ is symmetric positive definite.

Assumptions 1–4 ensure a well-defined differential inverse problem and a valid Fisher-information-based co-design objective.

4.3. Formal problem statement

The objective is to jointly design a differential spiral sensor geometry d and a frequency subset F such that the resulting differential impedance measurements maximize the worst-case inferential quality for recovering or distinguishing latent biofluid-state parameters $\theta \in \Theta$.

Formally, let $\mathbf{h}(d, F; \theta)$ denote the stacked real-imaginary mean differential response (defined in Section 4.9), and let $\mathcal{I}(\theta; d, F)$ be the Fisher information matrix (Section 4.10). The co-design problem is posed as the minimax program

$$(d^*, F^*) \in \arg \max_{\substack{d \in D \\ F \subset [\omega_{\min}, \omega_{\max}],\, |F| = m}} \min_{\theta \in \Theta} \Phi(\mathcal{I}(\theta; d, F)), \tag{4.4}$$

where Φ is an identifiability functional (e.g., D-optimal or E-optimal criterion).

The formulation in Eq. (4.4) yields a robust design optimized against the most adverse admissible latent configuration. In this study, that design is used for application-motivated synthetic validation, not for direct clinical claims.

4.4. Differential sensing architecture and measurement operator

4.4.1. Single-channel spiral measurement model (baseline operator)

Let $\mathcal{H}(d, \omega; \theta) \in \mathbb{C}$ denote the ideal impedance response of a spiral geometry d interrogating a medium parameterized by θ at angular frequency ω. Let $\nu \in \mathcal{V} \subset \mathbb{R}^r$ parameterize nuisance effects. A single-channel spiral measurement is modeled as

$$Z(d, \omega; \theta, \nu) = \mathcal{H}(d, \omega; \theta) + \mathcal{P}(d, \omega; \nu) + \epsilon(\omega), \tag{4.5}$$

where $\mathcal{P}(d, \omega; \nu)$ is a structured nuisance term and $\epsilon(\omega)$ is zero-mean complex noise.

Eq. (4.5) represents the conventional non-differential operator and serves as the mathematical baseline.

4.4.2. Proposed differential spiral architecture (sensor operator)

The proposed sensor uses two nominally co-located and nominally matched spiral channels on the same platform. The sensing spiral interacts with the unknown sample condition parameterized by θ, and the reference spiral interacts with a known reference condition parameterized by θ_r. This paired architecture is introduced as an idealized differential sensing configuration for methodological analysis, with practical performance expected to depend on the degree of physical matching achieved after fabrication and readout integration.

Their measured impedances are

$$Z_s(d, \omega) = \mathcal{H}(d, \omega; \theta) + \mathcal{P}(d, \omega; \nu) + \epsilon_s(\omega), \tag{4.6}$$

$$Z_r(d, \omega) = \mathcal{H}(d, \omega; \theta_r) + \mathcal{P}(d, \omega; \nu) + \epsilon_r(\omega). \tag{4.7}$$

The differential observable is defined by

$$\Delta Z(d, \omega) := Z_s(d, \omega) - Z_r(d, \omega). \tag{4.8}$$

Proposition 1 (*Common-Mode Nuisance Cancellation*)**.** *Under Assumptions 1–2, the differential measurement in Eq. (4.8) satisfies*

$$\Delta Z(d, \omega) = \Delta \mathcal{H}(d, \omega; \theta) + \xi(\omega), \tag{4.9}$$

where

$$\Delta \mathcal{H}(d, \omega; \theta) = \mathcal{H}(d, \omega; \theta) - \mathcal{H}(d, \omega; \theta_r), \tag{4.10}$$

and $\xi(\omega) = \epsilon_s(\omega) - \epsilon_r(\omega)$ is residual differential noise.

Subtract Eq. (4.7) from Eq. (4.6). By Assumption 1, the nuisance term $\mathcal{P}(d, \omega; \nu)$ cancels identically, yielding Eq. (4.9). □

Eq. (4.9) formalizes the key architectural idea: the measurement operator changes from a single-channel impedance map to a differential operator that suppresses common-mode nuisance under the stated matching assumptions. In practice, the extent of this suppression may be limited by residual asymmetry, parasitic imbalance, and other unmodeled non-ideal effects.

4.5. Physics-based forward operator for spiral impedance

For each (d, ω, θ), the ideal response $\mathcal{H}(d, \omega; \theta)$ is induced by a quasi-static complex-conductivity field model. Let $\phi : \Omega \to \mathbb{C}$ denote the complex potential solving

$$\nabla \cdot \big(\gamma(x, \omega; \theta)\nabla\phi(x)\big) = 0 \qquad \text{in } \Omega, \tag{4.11}$$

subject to electrode boundary conditions determined by the spiral geometry d:

$$\phi|_{\partial\Omega_d^{(+)}} = V, \tag{4.12}$$

$$\phi|_{\partial\Omega_d^{(-)}} = 0, \tag{4.13}$$

and insulating conditions elsewhere:

$$\gamma(x, \omega; \theta)\nabla\phi(x) \cdot n(x) = 0 \quad \text{on } \partial\Omega \setminus \big(\partial\Omega_d^{(+)} \cup \partial\Omega_d^{(-)}\big). \tag{4.14}$$

The complex current is

$$I(d, \omega; \theta) = \int_{\partial\Omega_d^{(+)}} \gamma(x, \omega; \theta)\nabla\phi(x) \cdot n(x)\, ds, \tag{4.15}$$

and the ideal impedance is

$$\mathcal{H}(d, \omega; \theta) = \frac{V}{I(d, \omega; \theta)}. \tag{4.16}$$

Eqs. (4.11)–(4.16) define the spiral forward map underlying the differential operator in Eq. (4.10). In this work, the operator is used as the generative core for synthetic mathematical validation.

4.6. Structured nuisance model (parasitics and drift)

To make the differential construction mathematically meaningful, the nuisance term in Eq. (4.5) is modeled as a structured parasitic operator rather than an unstructured perturbation. We write

$$\mathcal{P}(d, \omega; \nu) = j\omega L_\ell(d) + \frac{1}{j\omega C_s(d)} + Z_{\text{ep}}(\omega; \rho) + \delta_{\text{drift}}(\omega; \kappa), \tag{4.17}$$

where $\nu = (L_\ell, C_s, \rho, \kappa)$.

Here, $L_\ell(d)$ captures effective lead/interconnect inductance, $C_s(d)$ captures stray capacitance, $Z_{\text{ep}}(\omega; \rho)$ captures electrode-polarization-like effects, and $\delta_{\text{drift}}(\omega; \kappa)$ captures slow environmental or electronic drift.

A standard constant-phase-element (CPE) form may be used for Z_{ep}:

$$Z_{\text{ep}}(\omega; \rho) = \frac{1}{Q(j\omega)^\beta}, \qquad \rho = (Q, \beta), \quad Q > 0, \ \beta \in (0, 1). \tag{4.18}$$

The exact parametric form in Eqs. (4.17)–(4.18) is not essential to the theory. The key point is the structured common-mode character assumed in Assumption 1, which the differential sensor is designed to exploit. At the same time, this nuisance model should be interpreted as a structured surrogate for methodological analysis rather than as a complete representation of all non-ideal effects that may arise in fabricated biosensor hardware.

4.7. Latent biofluid-state parameterization (dispersive surrogate)

To obtain a finite-dimensional inverse-design problem, the interrogated sample is parameterized by a latent vector $\theta \in \Theta$. A physically interpretable choice for synthetic generation is a Cole–Cole-type model:

$$\varepsilon^*(\omega; \theta) = \varepsilon_\infty + \frac{\Delta\varepsilon}{1 + (j\omega\tau)^{1-\alpha}} + \frac{\sigma_0}{j\omega}, \qquad \theta = (\varepsilon_\infty, \Delta\varepsilon, \tau, \alpha, \sigma_0), \tag{4.19}$$

with constraints

$$\varepsilon_\infty > 0, \quad \Delta\varepsilon > 0, \quad \tau > 0, \quad \alpha \in (0, 1), \quad \sigma_0 \geq 0. \tag{4.20}$$

The corresponding complex admittivity in Eq. (4.1) is obtained from $\varepsilon^*(\omega; \theta)$ in the standard way.

In this paper, θ is an effective latent description of the biofluid state and should not be interpreted as a direct clinical biomarker vector. The reference branch parameter θ_r is fixed and known, and can represent a reference medium or a reference urine matrix. The methodology does not depend on the specific dispersive family and can be extended to alternative finite-dimensional parameterizations. However, the present validation remains limited to the assumed synthetic model family.

4.8. Synthetic uncertainty model for mathematical validation

Because this work establishes the sensor concept through synthetic evidence, the uncertainty sets and generative distributions are defined explicitly.

Latent-medium uncertainty set. Let

$$\Theta = \big\{\theta \in \mathbb{R}^p : \ \theta_{\min} \leq \theta \leq \theta_{\max}, \ C_\Theta(\theta) \leq 0\big\}, \tag{4.21}$$

where C_Θ encodes optional physical feasibility constraints (e.g., positivity, bounded relaxation exponent, parameter correlations).

Nuisance and tolerance uncertainty. Let $\nu \in \mathcal{V}$ and fabrication perturbations $\delta d \in \mathcal{U}$ be sampled from synthetic distributions supported on admissible sets:

$$\nu \sim \Pi_\nu, \qquad \delta d \sim \Pi_d, \qquad \tilde{d} = d + \delta d. \tag{4.22}$$

The same nuisance realization ν is applied to both sensing and reference channels to preserve common-mode structure, while residual mismatch is absorbed into $\Sigma(d, F)$.

Remark. This synthetic uncertainty specification is part of the mathematical problem definition. The robust co-design objective in Eq. (4.4) is interpreted over Θ and evaluated under nuisance and tolerance stress. In the present study, this remains application-motivated synthetic validation rather than experimental or clinical validation.

4.9. Observation model over a cardinality-constrained frequency subset

Let $F = \{\omega_k\}_{k=1}^m$ be a frequency subset. Using Eq. (4.9), the differential observation at each ω_k is

$$y_k = \Delta\mathcal{H}(d, \omega_k; \theta) + \xi_k, \qquad k = 1, \ldots, m, \tag{4.23}$$

where $y_k \in \mathbb{C}$ and $\xi_k \in \mathbb{C}$.

Define the real-valued stacked observation vector

$$\mathbf{y}(d, F) = \begin{bmatrix} \text{Re}(y_1) \\ \text{Im}(y_1) \\ \vdots \\ \text{Re}(y_m) \\ \text{Im}(y_m) \end{bmatrix} \in \mathbb{R}^{2m}, \tag{4.24}$$

and the corresponding mean response

$$\mathbf{h}(d, F; \theta) = \begin{bmatrix} \text{Re}\big(\Delta\mathcal{H}(d, \omega_1; \theta)\big) \\ \text{Im}\big(\Delta\mathcal{H}(d, \omega_1; \theta)\big) \\ \vdots \\ \text{Re}\big(\Delta\mathcal{H}(d, \omega_m; \theta)\big) \\ \text{Im}\big(\Delta\mathcal{H}(d, \omega_m; \theta)\big) \end{bmatrix} \in \mathbb{R}^{2m}. \tag{4.25}$$

The residual differential noise is modeled as

$$\xi = \begin{bmatrix} \mathrm{Re}(\xi_1) \\ \mathrm{Im}(\xi_1) \\ \vdots \\ \mathrm{Re}(\xi_m) \\ \mathrm{Im}(\xi_m) \end{bmatrix} \sim \mathcal{N}\big(0, \Sigma(d,F)\big), \tag{4.26}$$

with $\Sigma(d,F) \succ 0$ by Assumption 4. Therefore,

$$\mathbf{y}(d,F) = \mathbf{h}(d,F;\theta) + \xi. \tag{4.27}$$

4.10. Identifiability analysis via Fisher information

The local sensitivity of the differential mean response with respect to the latent biofluid-state parameters is quantified by the Jacobian

$$J(\theta;d,F) = \frac{\partial \mathbf{h}(d,F;\theta)}{\partial \theta} \in \mathbb{R}^{2m\times p}. \tag{4.28}$$

Under the Gaussian model in Eq. (4.27), the Fisher information matrix (FIM) is

$$\mathcal{I}(\theta;d,F) = J(\theta;d,F)^\top \Sigma(d,F)^{-1} J(\theta;d,F) \in \mathbb{R}^{p\times p}. \tag{4.29}$$

The Cramér–Rao inequality implies

$$\mathrm{Cov}(\widehat{\theta}) \succeq \mathcal{I}(\theta;d,F)^{-1} \tag{4.30}$$

for any unbiased estimator $\widehat{\theta}$, thereby justifying FIM-based co-design as a principled surrogate for inverse-problem conditioning.

4.10.1. Information improvement under differential covariance reduction

We formalize the effect of nuisance cancellation on inferential conditioning.

Proposition 2 (*FIM Monotonicity Under Covariance Dominance*). *Let $J \in \mathbb{R}^{2m\times p}$ be fixed. Suppose $\Sigma_1, \Sigma_2 \in \mathbb{R}^{2m\times 2m}$ are SPD matrices satisfying*

$$\Sigma_1 \preceq \Sigma_2. \tag{4.31}$$

Then

$$J^\top \Sigma_1^{-1} J \succeq J^\top \Sigma_2^{-1} J. \tag{4.32}$$

Proof. Since $\Sigma_1 \preceq \Sigma_2$ and both are SPD, the Loewner order reverses under inversion:

$$\Sigma_2^{-1} \preceq \Sigma_1^{-1}. \tag{4.33}$$

Pre- and post-multiplication by $J^\top$ and J preserves PSD order, yielding Eq. (4.32). □

In the proposed architecture, differential subtraction is designed to reduce the effective covariance relative to a single-channel spiral operator, which can increase the FIM in the sense of Eq. (4.32).

4.11. Robust identifiability criteria

We define two standard scalarizations of $\mathcal{I}(\theta;d,F)$.

D-optimal criterion.

$$\Phi_{\mathrm{D}}\big(\mathcal{I}\big) = \log\det\big(\mathcal{I} + \lambda I_p\big), \tag{4.34}$$

where $\lambda > 0$ is a stabilization parameter ensuring numerical regularity near singular regimes.

E-optimal criterion.

$$\Phi_{\mathrm{E}}\big(\mathcal{I}\big) = \lambda_{\min}(\mathcal{I}). \tag{4.35}$$

The D-optimal criterion measures aggregate information volume, while the E-optimal criterion protects the weakest identifiable direction. Both can be used in Eq. (4.4). In this study, the E-optimal criterion is the primary robustness target, and the D-optimal criterion is used as a complementary characterization.

4.12. Minimax co-design of geometry and frequency subset

Substituting Eq. (4.29) into Eq. (4.4), the robust co-design objective becomes

$$(d^*,F^*) \in \arg \max_{\substack{d\in D \\ F\subset[\omega_{\min},\omega_{\max}],\,|F|=m}} \min_{\theta\in\Theta} \Phi\big(J(\theta;d,F)^\top \Sigma(d,F)^{-1} J(\theta;d,F)\big). \tag{4.36}$$

Eq. (4.36) is mixed discrete–continuous and generally nonconvex. We therefore introduce a relaxation for the frequency-subset variable.

4.13. Frequency-subset relaxation and projection

Let $\{\widetilde{\omega}_\ell\}_{\ell=1}^M$ be a dense candidate frequency grid over $[\omega_{\min},\omega_{\max}]$, with $M \gg m$. Introduce weights $w = (w_1,\dots,w_M)^\top \in \mathbb{R}^M$ satisfying

$$0 \le w_\ell \le 1, \qquad \sum_{\ell=1}^M w_\ell = m. \tag{4.37}$$

Define the relaxed information matrix by additive decomposition:

$$\mathcal{I}(\theta;d,w) = \sum_{\ell=1}^M w_\ell\, \mathcal{I}_\ell(\theta;d), \tag{4.38}$$

where $\mathcal{I}_\ell(\theta;d)$ is the single-frequency FIM contribution at $\widetilde{\omega}_\ell$.

The relaxed minimax problem is

$$(d^*,w^*) \in \arg \max_{\substack{d\in D \\ w\in[0,1]^M,\ \sum_\ell w_\ell = m}} \min_{\theta\in\Theta} \Phi\big(\mathcal{I}(\theta;d,w)\big). \tag{4.39}$$

A discrete frequency subset is then recovered by the projection

$$F^* = \text{Top-}m\big(\{w_\ell^*\}_{\ell=1}^M\big), \tag{4.40}$$

which selects the m frequencies associated with the largest optimized weights.

4.14. Adversarial approximation of the inner minimization

The inner minimization over Θ in Eq. (4.39) is approximated by a finite adversarial scenario set $\{\theta^{(t)}\}_{t=1}^T \subset \Theta$:

$$\min_{\theta\in\Theta} \Phi\big(\mathcal{I}(\theta;d,w)\big) \approx \min_{1\le t\le T} \Phi\big(\mathcal{I}(\theta^{(t)};d,w)\big). \tag{4.41}$$

To tighten this approximation, each scenario is updated through projected descent in θ:

$$\theta^{(t)} \leftarrow \Pi_\Theta\big(\theta^{(t)} - \eta_\theta \nabla_\theta \Phi\big(\mathcal{I}(\theta^{(t)};d,w)\big)\big), \qquad t = 1,\dots,T, \tag{4.42}$$

where Π_Θ denotes projection onto Θ. This procedure iteratively concentrates the scenario set on hard-to-identify regions of the latent-parameter space.

4.15. Alternating optimization scheme

We solve Eq. (4.39) by alternating updates over geometry d and frequency weights w, with adversarial scenario refinement between the updates.

4.15.1. Geometry update

For fixed w and adversarial scenarios $\{\theta^{(t)}\}_{t=1}^T$, define the robust surrogate objective

$$\Psi(d;w) = \min_{1\le t\le T} \Phi\big(\mathcal{I}(\theta^{(t)};d,w)\big). \tag{4.43}$$

The geometry is updated by projected ascent:

$$d \leftarrow \Pi_D\big(d + \eta_d \nabla_d \Psi(d;w)\big). \tag{4.44}$$

Table 2
Shared experimental configuration for all methods.

Component	Setting reported for all methods
Operating band	$[\omega_{\min}, \omega_{\max}]$ (log-spaced candidate grid)
Candidate frequency grid	$\widetilde{\Omega} = \{\widetilde{\omega}_\ell\}_{\ell=1}^{M}$, with $M = 64$
Frequency budget	$m \in \{4, 6, 8\}$, identical across methods within each comparison block
Geometry design space	$d \in \mathcal{D}$ with fabrication and symmetry constraints
Latent biofluid-state model	Finite-dimensional dispersive model (Cole–Cole-type)
Latent uncertainty set	$\Theta = \{\theta : \theta_{\min} \le \theta \le \theta_{\max},\ C_\Theta(\theta) \le 0\}$
Reference branch	Fixed known parameter θ_r (same in optimization and test unless mismatch stress is enabled)
Nuisance model	Structured parasitic operator $\mathcal{P}(d, \omega; \nu)$ with $\nu \sim \Pi_\nu$
Tolerance model	$\delta d \sim \Pi_d$, manufactured geometry $\tilde{d} = d + \delta d$
Residual noise model	$\xi \sim \mathcal{N}(0, \Sigma(d, F))$
Data splits	Train/validation/test synthetic splits with non-overlapping sampled tuples
Randomness control	Fixed seeds + multi-seed reporting for final metrics

4.15.2. Frequency-weight update

For fixed d, define

$$\Xi(w; d) = \min_{1 \le t \le T} \Phi\big(\mathcal{I}(\theta^{(t)}; d, w)\big). \tag{4.45}$$

The frequency weights are updated by projected ascent onto the capped simplex in Eq. (4.37):

$$w \leftarrow \Pi_{\Delta_m}\big(w + \eta_w \nabla_w \Xi(w; d)\big), \tag{4.46}$$

where

$$\Delta_m = \left\{ w \in [0,1]^M : \sum_{\ell=1}^{M} w_\ell = m \right\}. \tag{4.47}$$

4.16. Synthetic-data generation as a mathematical validation operator

To establish the concept without experimental measurements, we define a synthetic data generator induced by the forward and nuisance operators. For each sampled tuple $(\theta, \nu, \delta d)$ and each frequency ω_k, we form

$$Z_s(\tilde{d}, \omega_k) = \mathcal{H}(\tilde{d}, \omega_k; \theta) + \mathcal{P}(\tilde{d}, \omega_k; \nu) + \epsilon_s(\omega_k), \tag{4.48}$$

$$Z_r(\tilde{d}, \omega_k) = \mathcal{H}(\tilde{d}, \omega_k; \theta_r) + \mathcal{P}(\tilde{d}, \omega_k; \nu) + \epsilon_r(\omega_k), \tag{4.49}$$

with $\tilde{d} = d + \delta d$ as in Eq. (4.22). The differential synthetic observation is then

$$\Delta Z(\tilde{d}, \omega_k) = Z_s(\tilde{d}, \omega_k) - Z_r(\tilde{d}, \omega_k). \tag{4.50}$$

Eq. (4.50) is the mathematical validation operator used to evaluate robust identifiability metrics and compare the proposed differential sensor against non-differential baselines under the same synthetic uncertainty model. Thus, the synthetic study is treated as a direct consequence of the methodology rather than as experimental validation.

4.17. Mathematical summary of the optimized quantity

The proposed framework optimizes a robust lower bound on the local inferential geometry of the differential spiral EIS biosensor inverse problem. It seeks a sensor–frequency pair (d, F) that maximizes the worst-case value of $\Phi(\mathcal{I}(\theta; d, F))$ across $\theta \in \Theta$.

The matrix $\mathcal{I}(\theta; d, F)$ is induced by a physics-based differential measurement operator, a structured common-mode nuisance model with residual differential covariance, a cardinality-constrained frequency-selection mechanism, and a synthetic uncertainty model used for application-motivated mathematical validation.

This methodology provides a principled route for sensor design through operator design (differential architecture) and experiment design (frequency co-selection), with synthetic evidence interpreted through a robust identifiability lens.

Algorithm 1 summarizes the proposed solver for the minimax co-design problem, using alternating projected updates for geometry and relaxed frequency variables with adversarial latent-scenario refinement.

Algorithm 1 Robust Differential Spiral Co-Design (Geometry + Frequency)

Require: Feasible geometry set $\mathcal{D}$; reference parameter θ_r; latent uncertainty set Θ; candidate frequency grid $\{\widetilde{\omega}_\ell\}_{\ell=1}^{M}$; frequency budget m; identifiability criterion Φ; number of adversarial scenarios T

Ensure: Co-designed geometry d^* and frequency subset F^*

Initialize $d^{(0)} \in \mathcal{D}$
Initialize $w^{(0)} \in \Delta_m$ with Δ_m defined in Eq. (4.47)
Initialize adversarial scenarios $\{\theta^{(t,0)}\}_{t=1}^{T} \subset \Theta$
Set iteration counter $k \leftarrow 0$
for $k = 0, 1, 2, \ldots$ **until convergence**
  Geometry update
    Form $\mathcal{I}(\theta^{(t,k)}; d^{(k)}, w^{(k)})$ using Eq. (4.38)
    Compute $\Psi(d; w^{(k)})$ as in Eq. (4.43)
    Update $d^{(k+1)}$ by projected ascent using Eq. (4.44)
  Frequency-weight update
    Form $\mathcal{I}(\theta^{(t,k)}; d^{(k+1)}, w)$ using Eq. (4.38)
    Compute $\Xi(w; d^{(k+1)})$ as in Eq. (4.45)
    Update $w^{(k+1)}$ by projected ascent using Eq. (4.46)
  Adversarial scenario refinement
    for all $t \in \{1, \ldots, T\}$
      Update $\theta^{(t,k+1)}$ by projected descent using Eq. (4.42)
    end for
  Stopping criterion
    if $\|d^{(k+1)} - d^{(k)}\|_2 \le \epsilon_d$ **and** $\|w^{(k+1)} - w^{(k)}\|_2 \le \epsilon_w$
      break
    end if
end for
Compute $F^* = \text{Top-}m(\{w_\ell^{(k+1)}\}_{\ell=1}^{M})$ using Eq. (4.40)
Set $d^* = d^{(k+1)}$
return (d^*, F^*)

5. Experimental setup

5.1. Protocol overview

The primary co-design experiments use synthetic data generated from the forward and nuisance operators in Section 4. This protocol isolates the effects of the differential sensor operator and geometry–frequency co-design under one shared uncertainty model; all compared methods use the same uncertainty sets, nuisance/tolerance distributions, candidate frequency grid, and frequency budget.

The synthetic evaluation asks whether differential sensing improves robustness over a single-channel spiral operator, whether co-design improves identifiability over fixed-geometry or heuristic-frequency choices, and whether these gains remain stable under stress. A separate measured-data analysis, described in Section 5.10, evaluates only the transferability of the differential sparse-frequency principle outside the synthetic model family. Neither analysis constitutes clinical validation.

Table 3
Compared baselines and the proposed method (shared synthetic uncertainty model, candidate grid, and evaluation protocol).

ID	Operator	Geometry	Frequencies
B1	Single (Z_s)	Fixed	Uniform log-spaced
B2	Single (Z_s)	Fixed	Heuristic
B3	Differential (ΔZ)	Fixed	Uniform log-spaced
B4	Differential (ΔZ)	Fixed	Heuristic
B5	Differential (ΔZ)	Fixed	Co-designed
B6	Differential (ΔZ)	Co-designed	Heuristic
B7	Differential (ΔZ)	Fixed	Greedy D-optimal
B8	Differential (ΔZ)	Fixed	Greedy E-optimal
Ours	Differential (ΔZ)	Co-designed	Co-designed

5.2. Synthetic data generation model

For each synthetic trial, a latent biofluid-state parameter $\theta \sim \Pi_\Theta$, nuisance parameter $\nu \sim \Pi_\nu$, and fabrication perturbation $\delta d \sim \Pi_d$ are sampled, and the manufactured geometry is $\tilde{d} = d + \delta d$.

The sensing response is generated as

$$Z_s(\tilde{d}, \omega_k) = \mathcal{H}(\tilde{d}, \omega_k; \theta) + \mathcal{P}(\tilde{d}, \omega_k; \nu) + \epsilon_s(\omega_k), \tag{5.1}$$

and the reference response is generated as

$$Z_r(\tilde{d}, \omega_k) = \mathcal{H}(\tilde{d}, \omega_k; \theta_r) + \mathcal{P}(\tilde{d}, \omega_k; \nu) + \epsilon_r(\omega_k). \tag{5.2}$$

The differential observation is

$$\Delta Z(\tilde{d}, \omega_k) = Z_s(\tilde{d}, \omega_k) - Z_r(\tilde{d}, \omega_k). \tag{5.3}$$

The same nuisance realization ν is applied to both branches in each trial to preserve the assumed common-mode structure of the differential operator.

5.3. Experimental factors and shared constraints

The geometry variable is the same as in Section 4,

$$d = \left(N, w, s, D_{\text{out}}, t_{\text{sub}}, \epsilon_{\text{sub}}, g, w_g\right) \in D, \tag{5.4}$$

and the selected frequency subset satisfies

$$F = \{\omega_k\}_{k=1}^{m} \subset \widetilde{\Omega}, \qquad |F| = m, \tag{5.5}$$

where $\widetilde{\Omega} = \{\widetilde{\omega}_\ell\}_{\ell=1}^{M}$ is a logarithmically spaced candidate grid unless otherwise stated.

Matched-layout constraints are imposed on the sensing and reference branches (mirrored routing, matched pads, and matched interconnect length) to preserve the intended differential validity. All methods are evaluated with identical M, m, Θ, Π_Θ, Π_ν, and Π_d.

Table 2 summarizes the shared experimental configuration.

5.4. Compared methods and baseline definitions

The comparison protocol is organized along three axes: sensor operator, frequency selection, and geometry design. Table 3 defines the baselines, the stronger frequency-selection comparators, and the proposed configuration. All methods use the same synthetic data generator and the same measurement budget.

For B2, B4, and B6, the heuristic subset is selected by a fixed non-iterative rule on the training/co-design split (e.g., sensitivity-magnitude or variance ranking). For B7 and B8, the frequency subset is selected by stronger greedy design criteria applied on the same split, using D-optimal and E-optimal selection rules, respectively. The proposed subset is obtained by relaxed minimax optimization followed by top-m projection.

5.5. Default hyperparameters for co-design and baselines

To improve reproducibility and avoid hidden tuning advantages, Table 4 lists the default hyperparameters used for the proposed optimization and the baseline procedures. These values are fixed before final test evaluation and tuned only on the validation split.

5.6. Data splits and fairness protocol

Synthetic samples are partitioned into disjoint train, validation, and test splits. The sampled tuples $(\theta, \nu, \delta d)$ do not overlap across splits, and no exact realization used in co-design or tuning is reused in the test set. Hyperparameters in Table 4 are selected on the validation split only.

All methods share the same candidate frequency grid $\widetilde{\Omega}$, frequency budget m, uncertainty distributions $(\Pi_\Theta, \Pi_\nu, \Pi_d)$, split construction, and Monte Carlo budget on the test set. This fairness rule is enforced in every reported experiment.

5.7. Evaluation metrics

The evaluation follows the methodological objective of robust identifiability. The primary metric is the worst-case E-optimal score

$$\mathcal{M}_{\text{E}}(d, F) = \min_{\theta \in \Theta} \lambda_{\min}\left(\mathcal{I}(\theta; d, F)\right), \tag{5.6}$$

and the secondary metric is the worst-case D-optimal score

$$\mathcal{M}_{\text{D}}(d, F) = \min_{\theta \in \Theta} \log\det\left(\mathcal{I}(\theta; d, F) + \lambda I\right). \tag{5.7}$$

We also report the CRLB proxy trace metric

$$\mathcal{M}_{\text{tr}}(d, F) = \max_{\theta \in \Theta} \operatorname{trace}\left(\mathcal{I}(\theta; d, F)^{-1}\right), \tag{5.8}$$

the CRLB proxy spectral metric

$$\mathcal{M}_{\text{spec}}(d, F) = \max_{\theta \in \Theta} \left\|\mathcal{I}(\theta; d, F)^{-1}\right\|_2, \tag{5.9}$$

and the frequency-efficiency quantity

$$m^\star = \min\left\{m : \ \mathcal{M}_{\text{E}}(d, F) \geq \tau_{\text{id}}\right\}. \tag{5.10}$$

All summary statistics are reported on the held-out test set across multiple random seeds.

5.8. Stress-test protocol

Robustness is tested under nuisance amplification, tolerance amplification, and optional reference mismatch. Under nuisance amplification, an inflated nuisance distribution $\Pi_\nu^{(\alpha)}$ with factor $\alpha > 1$ is used, and degradation is reported as

$$\text{Deg}_{\mathcal{Q}}(\alpha) = \frac{\mathcal{Q}(d, F; \Pi_\nu^{(\alpha)}) - \mathcal{Q}(d, F; \Pi_\nu)}{\left|\mathcal{Q}(d, F; \Pi_\nu)\right|}. \tag{5.11}$$

An analogous protocol is used for tolerance amplification by inflating Π_d. When reference mismatch is studied, the test-time reference is perturbed as

$$\theta_r^{\text{test}} = \theta_r + \delta\theta_r. \tag{5.12}$$

5.9. Reproducibility checklist

The final manuscript reports the numerical values used for the frequency band, grid size, budgets, uncertainty ranges, nuisance and tolerance distributions, optimization parameters, split sizes, and random seeds.

This is important because the main geometry co-design evidence is synthetic, and its strength depends on clear reporting of the generative and optimization assumptions.

Table 4
Default hyperparameters for the proposed co-design and baseline procedures.

Hyperparameter	Symbol	Default	Notes
Candidate grid size	M	64	Shared across all methods (log-spaced grid)
Frequency budget	m	$\{4, 6, 8\}$	Same m within each comparison block
Adversarial scenarios	T	16	Inner minimization approximation
Max outer iterations	$K_{\max}$	100	Alternating co-design loop
Geometry step size	η_d	5×10^{-3}	Projected ascent update
Frequency-weight step size	η_w	1×10^{-1}	Projected ascent on capped simplex
Adversarial step size	η_θ	1×10^{-2}	Projected descent in Θ
Geometry tolerance stop	ϵ_d	10^{-4}	Convergence threshold
Weight tolerance stop	ϵ_w	10^{-4}	Convergence threshold
D-opt stabilization	λ	10^{-6}	Used when reporting Φ_D
Primary criterion	Φ	Φ_E	E-optimal used as main robustness target
Initialization (weights)	$w^{(0)}$	m/M	Uniform initialization on capped simplex
Initialization (geometry)	$d^{(0)}$	Nominal feasible spiral	Shared nominal template for fair starts
Heuristic baseline ranking rule	–	Sensitivity-magnitude ranking	Fixed non-iterative rule on training split
Heuristic baseline tie-break	–	Ascending ω index	Deterministic tie handling
Monte Carlo trials (test)	N_{MC}	1000	Same for all methods
Random seeds	–	$\{11, 22, 33, 44, 55\}$	Shared seed protocol across methods

5.10. Independent measured-data validation protocol

To assess component-level transfer beyond the synthetic forward model, we analyzed the publicly available supplementary EIS measurements reported by Huerta-Nuñez et al. [29]. The dataset contains measured impedance magnitude and phase at 101 frequencies from 100 Hz to 1 MHz for three breast-cancer cell lines (MCF-7, MDA-MB-231, and SK-BR-3), together with antibody-matched nanoprobe–PBS controls. The source study used 50 cells in 500 µL of PBS and provided three biological samples with three repeated spectra per sample.

Complex impedance was reconstructed as $Z(\omega) = |Z(\omega)| \exp(j\phi(\omega))$. For each matched cell/control spectrum, the normalized cell-associated differential response was

$$\mathbf{x}^{+}(\omega) = \frac{Z_{\mathrm{cell}}(\omega) - Z_{\mathrm{control}}(\omega)}{|Z_{\mathrm{control}}(\omega)|}. \tag{5.13}$$

Measured background variability was represented by cyclic differences between control repeats,

$$\mathbf{x}^{0}(\omega) = \frac{Z_{\mathrm{control},r+1}(\omega) - Z_{\mathrm{control},r}(\omega)}{|Z_{\mathrm{control},r}(\omega)|}, \tag{5.14}$$

where the repeat index was cycled within each biological sample. This produced 27 cell-associated responses and 27 control-repeat responses; the latter are a repeatability reference, not a clinical negative cohort.

Evaluation used grouped leave-one-sample-out validation. All repeated spectra from the held-out sample were excluded from both selection and model fitting. Within each training fold, frequencies were selected greedily at budgets $m \in \{4, 6, 8\}$ by maximizing an empirical minimax Fisher-separation criterion computed from the real and imaginary differential features. A standardized logistic-regression classifier was then fitted on the selected features and evaluated on the held-out sample. Log-uniform subsets at the same budgets and the complete 101-frequency spectrum were used as comparators. Balanced accuracy, AUROC, F1 score, and accuracy were summarized as mean ± standard deviation across the three grouped folds. This experiment tests the differential sparse-frequency design principle on out-of-family measured spectra; it does not validate the optimized spiral geometry or transfer the exact synthetic frequency set unchanged. The measured-data preprocessing script is provided as Supplementary Code S1, the complete validation workflow as Supplementary Code S2, and the processed measured-EIS dataset as Supplementary Data S1.

6. Results

6.1. Main robust identifiability comparison

Table 5 shows the main comparison at a fixed frequency budget ($m = 6$). The proposed full differential co-design (Ours) gives the best overall robust-identifiability performance in this synthetic setting. It achieves the highest worst-case E-optimal and D-optimal scores and the lowest CRLB proxy values among all compared methods. Compared with the single-channel baseline (B1), the gains remain substantial across all reported metrics under the same budget and uncertainty model.

Table 5
Main robust-identifiability comparison across baselines and the proposed method under the shared synthetic uncertainty model (fixed frequency budget, $m = 6$). Arrows indicate whether higher (↑) or lower (↓) values are better.

Method	$\mathcal{M}_{\mathrm{E}}$ ↑	$\mathcal{M}_{\mathrm{D}}$ ↑	$\mathcal{M}_{\mathrm{tr}}$ ↓	$\mathcal{M}_{\mathrm{spec}}$ ↓
B1	0.086	1.95	37.8	20.9
B2	0.094	2.06	35.1	18.7
B3	0.126	2.39	28.6	15.2
B4	0.137	2.57	25.4	13.6
B5	0.171	3.01	21.3	10.8
B6	0.166	3.08	20.1	11.2
B7	0.178	3.12	19.6	10.3
B8	0.183	3.09	19.1	9.9
Ours	**0.204**	**3.36**	**16.8**	**8.7**

Table 6
Frequency-budget efficiency comparison under the shared synthetic uncertainty model. To avoid duplication, the table reports the low- and high-budget cases ($m = 4$ and $m = 8$), while the $m = 6$ results are already reported in Table 5. Higher $\mathcal{M}_{\mathrm{E}}$ and $\mathcal{M}_{\mathrm{D}}$ are better; lower $\mathcal{M}_{\mathrm{tr}}$ is better.

Method	m	$\mathcal{M}_{\mathrm{E}}$ ↑	$\mathcal{M}_{\mathrm{D}}$ ↑	$\mathcal{M}_{\mathrm{tr}}$ ↓
B1	4	0.066	1.61	46.8
B1	8	0.098	2.14	33.2
B4	4	0.109	2.21	31.7
B4	8	0.151	2.79	22.6
B5	4	0.143	2.67	24.9
B5	8	0.186	3.18	19.6
B6	4	0.136	2.74	23.8
B6	8	0.182	3.26	18.4
Ours	4	**0.176**	**2.98**	**21.0**
Ours	8	**0.219**	**3.52**	**15.4**

The added stronger frequency-selection baselines B7 and B8 improve over the heuristic differential baseline B4 and remain competitive with the partial co-design variants B5 and B6, but neither matches the full co-design across all metrics. B7 is slightly stronger in $\mathcal{M}_{\mathrm{D}}$, whereas B8 is slightly better in $\mathcal{M}_{\mathrm{E}}$ and $\mathcal{M}_{\mathrm{spec}}$. This again indicates that different selection criteria emphasize different aspects of local identifiability. Fig. 2 shows this metric-wise behavior, and Fig. 3 confirms that the proposed method remains best overall after aggregation across metrics.

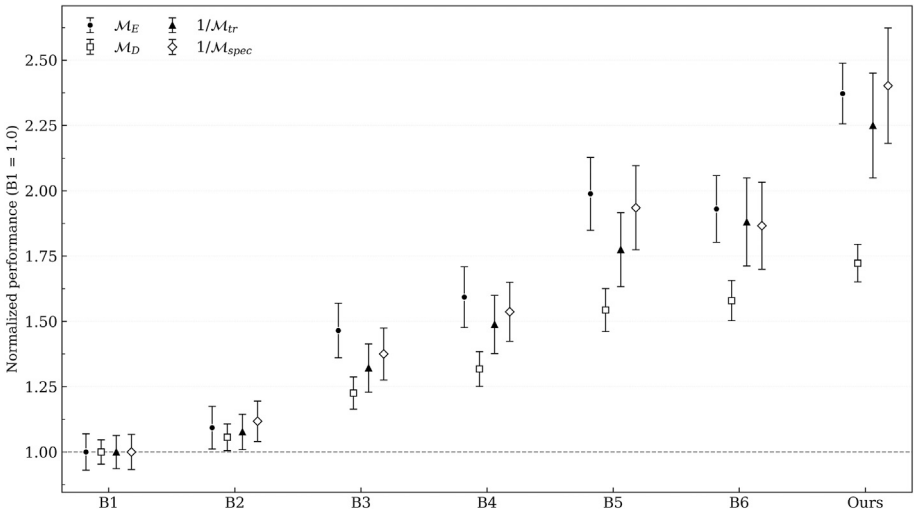

Fig. 2. Metric-wise normalized identifiability performance (B1 as reference, mean ± s.d. across seeds). The proposed full differential co-design shows the strongest overall profile, while intermediate baselines show metric-dependent trade-offs, especially between the frequency-only and geometry-only co-design variants.

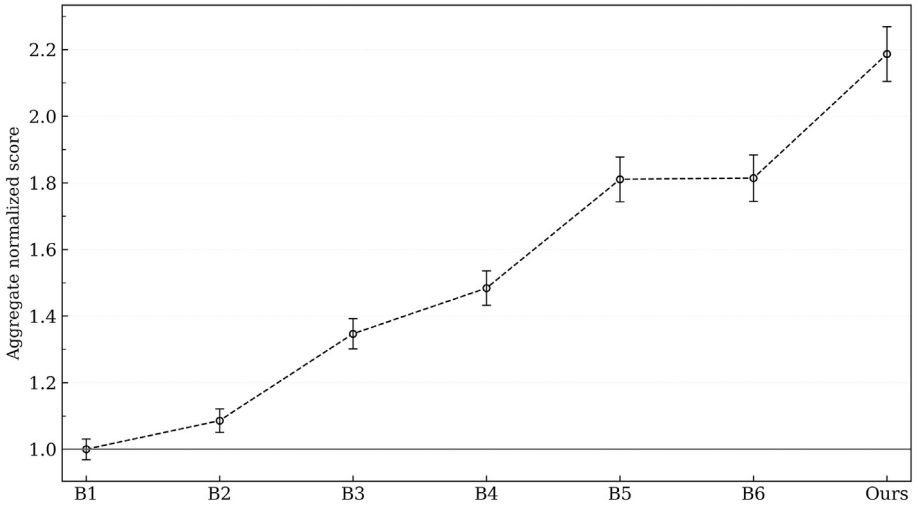

Fig. 3. Aggregate identifiability gain computed as the mean normalized score across the four reported metrics. This aggregate view is a compact summary and should be interpreted together with the metric-wise results in Fig. 2.

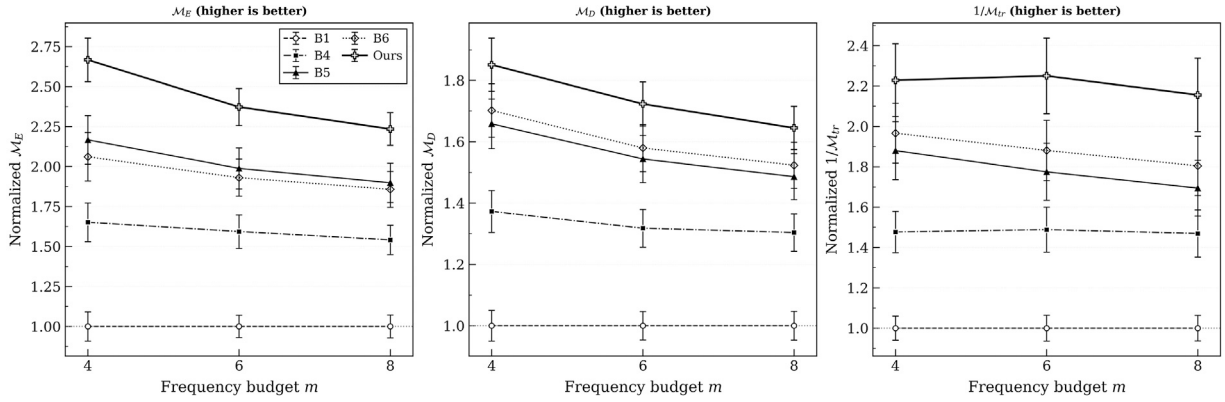

Fig. 4. Frequency-budget curves for representative metrics under the shared synthetic uncertainty model. The proposed method maintains a favorable performance–budget trade-off across all tested budgets and exhibits stronger performance at low budgets ($m = 4$) than all compared baselines.

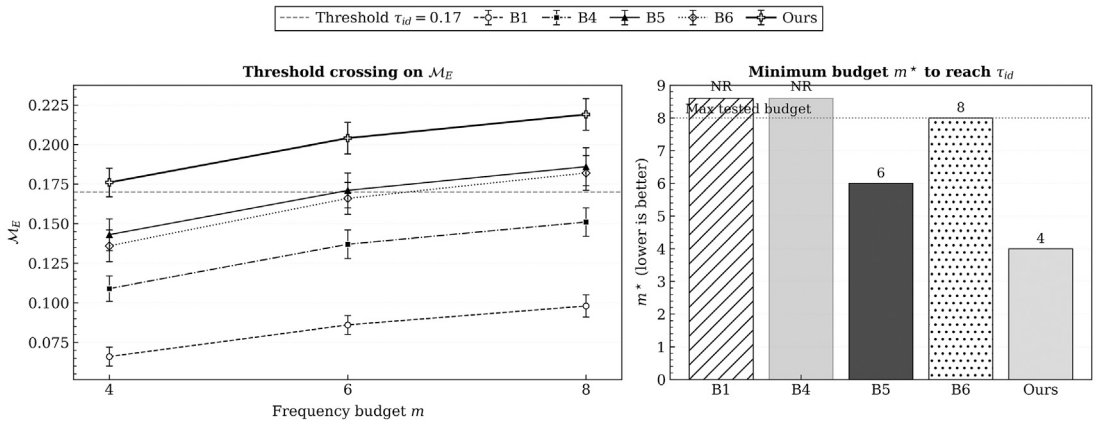

Fig. 5. Budget-efficiency summary using an identifiability threshold criterion. The proposed method reaches the target robust-identifiability level at a lower frequency budget than the baseline configurations, indicating improved measurement efficiency.

Table 7
Ablation definitions used in this subsection at fixed frequency budget ($m = 6$). To avoid repeating numerical results, the corresponding metric values are taken from Table 5.

Method	Ablation role
B1	Single-channel baseline
B3	Differential operator only
B4	Differential + heuristic frequencies
B5	Differential + frequency co-design (fixed geometry)
B6	Differential + geometry co-design (heuristic frequencies)
Ours	Full differential co-design (geometry + frequencies)

6.2. Frequency-budget efficiency analysis

Table 6, together with Table 5, shows how performance changes as the frequency budget increases from $m = 4$ to $m = 8$. All methods improve when more frequencies are used, but the improvement is not equal across methods. The proposed method remains the best at both low and high budgets, and it also leads at the intermediate budget ($m = 6$) reported earlier.

The low-budget case is especially important because it reflects measurement efficiency. At $m = 4$, the proposed method already outperforms all compared baselines in the reported metrics, which indicates that the full co-design can achieve strong identifiability with fewer interrogations. This is consistent with the performance–budget trends shown in Fig. 4.

The comparison between B5 and B6 again shows a metric-dependent trade-off. B6 is slightly stronger in $\mathcal{M}_D$ and $\mathcal{M}_{tr}$, while B5 remains competitive in $\mathcal{M}_E$, especially at lower budgets. The full co-design combines these advantages and gives the best overall performance–budget profile. Fig. 5 further supports this result by showing that the proposed method reaches the target identifiability threshold at a lower frequency budget than the baselines.

6.3. Ablation study: differential operator and co-design components

Table 7 defines the ablation roles used in this subsection, and the corresponding raw metric values at $m = 6$ are reported in Table 5. The ablation analysis isolates the effects of the differential operator, frequency co-design, and geometry co-design. Moving from B1 to B3 improves all reported metrics, which is consistent with better suppression of common-mode nuisance in the differential setting. The step from B3 to B4 gives a smaller additional gain, showing that the differential operator is the main architectural improvement before co-design is added.

B5 and B6 then separate the two co-design components. Both are clearly better than B4, but neither is best in every metric. B5 is slightly better in $\mathcal{M}_E$ and $\mathcal{M}_{spec}$, while B6 is slightly better in $\mathcal{M}_D$ and $\mathcal{M}_{tr}$. This indicates that frequency selection and geometry design improve different aspects of identifiability rather than giving the same gain.

The proposed method combines both co-design components and gives the strongest overall ablation result. Fig. 6 shows this in normalized metric-wise form, and Fig. 7 confirms that the full co-design achieves the best normalized score across the reported metrics among the ablation-focused methods. Overall, the ablation results support the main claim that the performance gain comes from the joint use of the differential operator and coupled geometry–frequency co-design.

Table 8
Robustness comparison under nuisance/tolerance amplification at fixed frequency budget $m = 6$. To avoid duplication, the default case ($\kappa = 1$) is reported in Table 5; this table reports amplified settings only. The amplification factor κ scales the synthetic nuisance covariance and fabrication-tolerance perturbation magnitudes relative to the default setting.

Method	κ	$\mathcal{M}_E \uparrow$	$\mathcal{M}_D \uparrow$	$\mathcal{M}_{tr} \downarrow$	$\mathcal{M}_{spec} \downarrow$
B4	1.5	0.124	2.33	28.7	15.4
B4	2.0	0.112	2.11	32.1	17.5
B4	2.5	0.101	1.95	35.6	19.2
B5	1.5	0.156	2.78	23.8	12.1
B5	2.0	0.142	2.53	26.7	13.7
B5	2.5	0.130	2.31	29.8	15.6
B6	1.5	0.150	2.84	22.6	12.8
B6	2.0	0.136	2.60	25.4	14.5
B6	2.5	0.123	2.38	28.7	16.6
Ours	1.5	**0.187**	**3.13**	**18.9**	**9.9**
Ours	2.0	**0.171**	**2.90**	**21.5**	**11.4**
Ours	2.5	**0.156**	**2.67**	**24.4**	**13.1**

6.4. Robustness under nuisance and tolerance amplification

Table 8, together with the default values in Table 5, shows the effect of increasing nuisance and fabrication-tolerance uncertainty. As κ increases, all methods degrade in identifiability scores and CRLB proxies. This is expected because stronger nuisance and tolerance perturbations make the inverse problem harder.

Despite this degradation, the proposed full differential co-design remains the best-performing method at all tested amplification levels. It keeps the highest $\mathcal{M}_E$ and $\mathcal{M}_D$ values and the lowest $\mathcal{M}_{tr}$ and $\mathcal{M}_{spec}$ values across the full sweep. Fig. 8 shows the same trend in curve form and indicates a more favorable degradation profile for the proposed method.

The ablation variants B5 and B6 remain clearly stronger than the heuristic differential baseline B4, but they keep different strengths under amplified uncertainty. B6 is slightly stronger in $\mathcal{M}_D$ and $\mathcal{M}_{tr}$, while

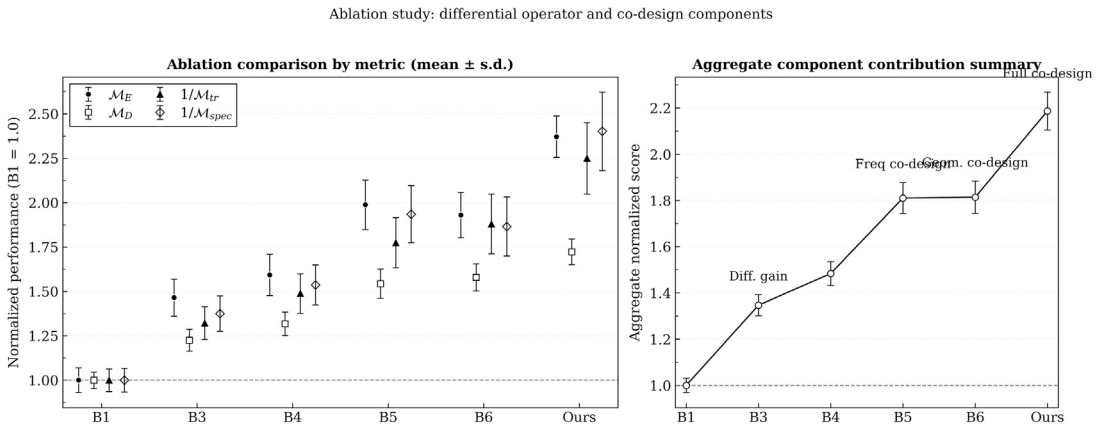

Fig. 6. Ablation comparison at $m = 6$. Left: metric-wise normalized performance (B1 as reference, mean ± s.d. across seeds). Right: aggregate normalized score used only as a compact summary.

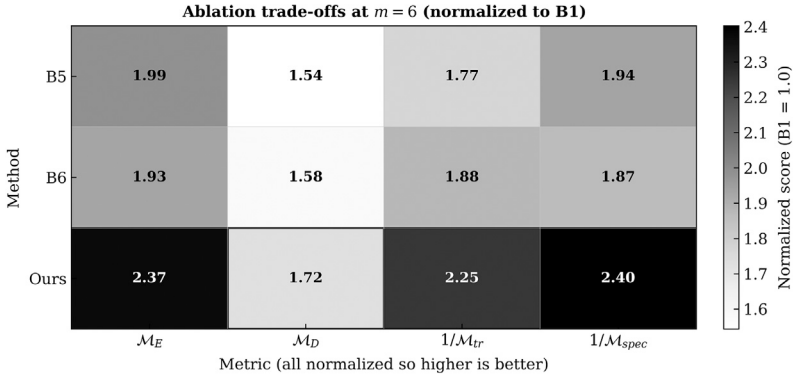

B5: frequency-only co-design; B6: geometry-only co-design; Ours: full co-design

Fig. 7. Heatmap summary of normalized ablation trade-offs at $m = 6$ (B5, B6, and Ours; all values normalized to B1 so higher is better). The highlighted cells indicate the best method per metric.

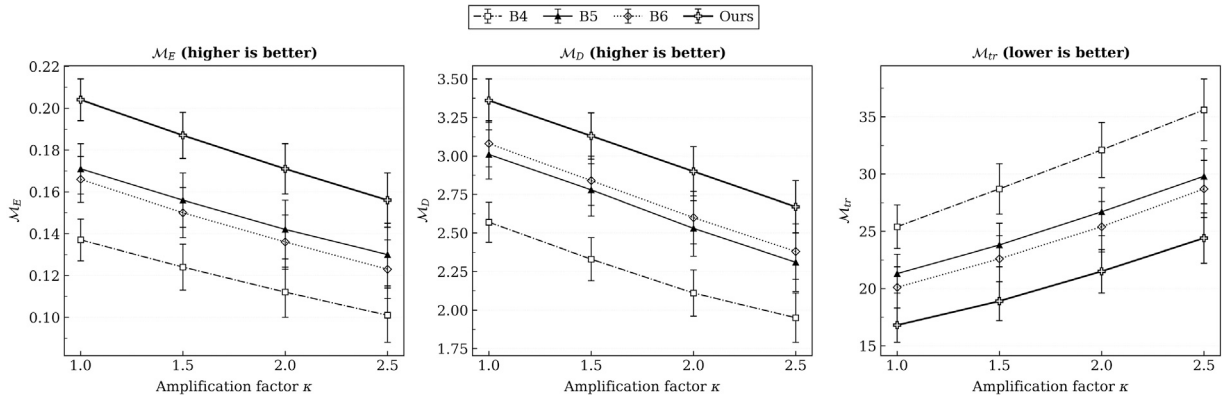

Fig. 8. Robustness curves under nuisance/tolerance amplification (κ) at fixed frequency budget $m = 6$. All methods degrade as κ increases, while the proposed method maintains the strongest overall performance across the reported metrics.

B5 remains competitive in $\mathcal{M}_{\mathrm{E}}$ and $\mathcal{M}_{\mathrm{spec}}$. This pattern is consistent with the earlier ablation and main-comparison results.

Fig. 9 provides a scale-independent summary using retention relative to $\kappa = 1$. Under this view, the proposed method shows the strongest overall retention, which means that its advantage is not limited to the default uncertainty setting. These results support the claim that the proposed differential geometry–frequency co-design improves both identifiability and robustness under stronger nuisance and tolerance perturbations.

6.5. Reference-mismatch sensitivity analysis

Table 9, together with the nominal values in Table 5, shows the effect of increasing reference-channel mismatch. As ρ increases, all differential methods degrade. This is expected because reference mismatch weakens common-mode cancellation and adds residual asymmetry to the differential measurement.

Despite this degradation, the proposed full differential co-design remains the best-performing method at every tested mismatch level.

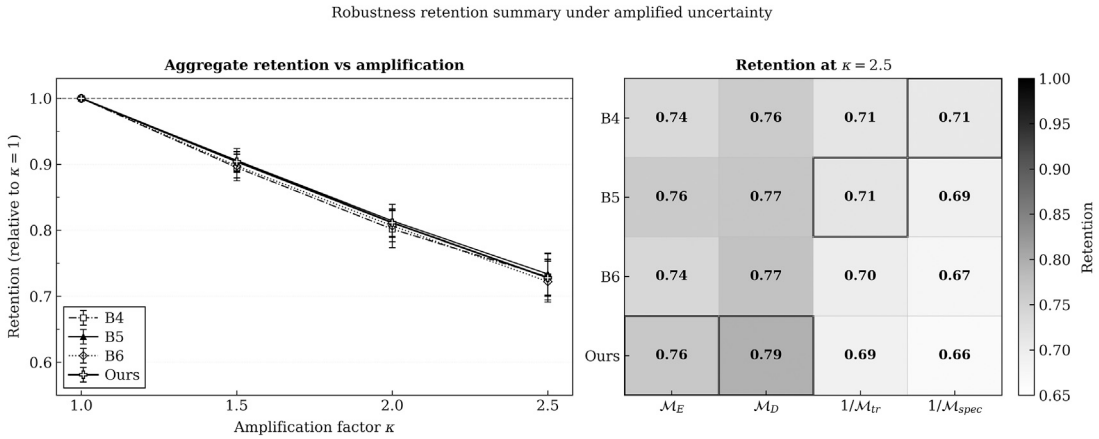

Fig. 9. Retention summary under amplified uncertainty, reported as performance retained relative to the default setting ($\kappa = 1$). Higher retention indicates more graceful degradation under nuisance/tolerance amplification.

Table 9
Reference-mismatch sensitivity at fixed frequency budget ($m = 6$). To avoid duplication, the nominal case ($\rho = 0$) is reported in Table 5; this table reports mismatch settings only. The mismatch factor ρ scales synthetic reference-channel deviations relative to the nominal differential setting. Raw metrics are reported together with aggregate retention (relative to $\rho = 0$; higher is better).

Method	ρ	$\mathcal{M}_E \uparrow$	$\mathcal{M}_D \uparrow$	$\mathcal{M}_{tr} \downarrow$	$\mathcal{M}_{spec} \downarrow$	Agg. ret. ↑
B4	0.1	0.132	2.46	26.8	14.3	0.955
B4	0.2	0.126	2.34	28.4	15.2	0.905
B4	0.3	0.119	2.21	30.2	16.1	0.854
B5	0.1	0.164	2.89	22.5	11.5	0.951
B5	0.2	0.156	2.75	24.1	12.5	0.894
B5	0.3	0.147	2.61	25.9	13.6	0.836
B6	0.1	0.159	2.95	21.4	12.0	0.947
B6	0.2	0.151	2.82	22.9	13.0	0.892
B6	0.3	0.142	2.67	24.8	14.2	0.830
Ours	0.1	**0.197**	**3.25**	**17.8**	**9.3**	**0.953**
Ours	0.2	**0.188**	**3.10**	**19.2**	**10.2**	**0.893**
Ours	0.3	**0.178**	**2.95**	**20.9**	**11.3**	**0.831**

It keeps the highest identifiability scores and the lowest CRLB proxies across the full mismatch sweep.

The co-design ablations B5 and B6 also remain stronger than the heuristic differential baseline B4, but they keep the same metric-dependent trade-off seen earlier. B6 is generally stronger in $\mathcal{M}_D$ and $\mathcal{M}_{tr}$, while B5 remains competitive in $\mathcal{M}_E$ and $\mathcal{M}_{spec}$.

The aggregate-retention column provides a compact summary relative to $\rho = 0$. It shows that the proposed method has the highest retention at mild mismatch ($\rho = 0.1$), and it remains close to the strongest ablations at larger mismatch levels. Overall, these results show that the proposed differential geometry–frequency co-design keeps a robust advantage even when reference matching is not ideal.

6.6. Computational cost and optimization overhead

Table 10 summarizes the optimization overhead of the main differential configurations and the added stronger frequency-selection baselines, using runtime normalized to B4. As expected, the proposed full co-design method has the highest cost because it jointly updates geometry and frequency variables and also refines adversarial latent-parameter scenarios.

The greedy baselines B7 and B8 increase cost only moderately relative to B4, since they optimize the frequency subset without full alternating co-design. The partial co-design baselines B5 and B6 already increase runtime relative to B4, which shows that optimizing even one component adds computational cost. The full method adds more overhead because it couples both updates and uses a larger adversarial refinement budget.

These results should be interpreted as an offline design-time comparison under the present synthetic setup, not as a real-time deployment benchmark. This cost should be interpreted together with the identifiability and robustness gains reported in the previous sections. In particular, the current runtime summary reflects the adopted synthetic forward model and optimization workflow; extension to higher-fidelity 3D geometries or denser discretizations would increase both computational time and memory demand and is left for future work. In this study, the proposed framework is intended as an offline sensor–protocol design tool, not as a real-time inference method.

6.7. Independent validation on measured EIS data

The measured spectra showed cell-line-specific differential patterns relative to the control-repeat variability band (Fig. 10), confirming that the external measurements contained nontrivial differential information not generated by the synthetic forward model. Across frequency budgets $m = 4$, 6, and 8, the training-only minimax subsets achieved mean balanced accuracies of 79.6%, 77.8%, and 75.9%, respectively, compared with 70.4%, 72.2%, and 68.5% for log-uniform subsets (Fig. 11). The full 101-frequency reference achieved 74.1% ± 8.5% balanced accuracy. At $m = 4$, the minimax subset achieved 79.6% ± 11.6% balanced accuracy and an AUROC of 0.716 ± 0.240, versus 70.4% ± 14.0% and 0.671 ± 0.164, respectively, for log-uniform selection; the corresponding full-spectrum AUROC was 0.712 ± 0.213.

These results provide independent, component-level evidence that differential sparse-frequency interrogation can retain useful information on measured spectra outside the synthetic formulation. The variability across the three grouped folds is substantial, so the numerical differences are descriptive and are not interpreted as proof of statistical superiority. Moreover, the experiment validates neither the optimized spiral geometry nor urine- or bladder-cancer-specific performance because the external data were acquired from breast-cancer cell suspensions using a different electrode platform.

7. Discussion

The results support the main methodological claim of this study. Robust identifiability improves when the sensing operator is differential and when geometry and frequency selection are optimized together. At the same frequency budget ($m = 6$), the proposed method gives the best values across all reported metrics in Table 5. This pattern remains

Table 10
Computational-cost summary at fixed frequency budget ($m = 6$) under the shared synthetic protocol. Runtime is reported as relative wall-clock time normalized to B4 (=1.00×), because absolute timing depends on implementation and hardware.

Method	Optimization content	Outer iterations	Inner/adversarial updates	Relative runtime	Memory trend
B4	Differential + heuristic frequency subset (no iterative co-design)	–	–	1.00×	Low
B7	Differential + greedy D-optimal frequency selection	6	–	1.41×	Low–Moderate
B8	Differential + greedy E-optimal frequency selection	6	–	1.47×	Low–Moderate
B5	Differential + frequency co-design (fixed geometry)	40	8 per outer iter.	2.35×	Moderate
B6	Differential + geometry co-design (heuristic frequencies)	45	8 per outer iter.	2.72×	Moderate
Ours	Full differential co-design (geometry + frequency)	60	12 per outer iter.	4.18×	Moderate–High

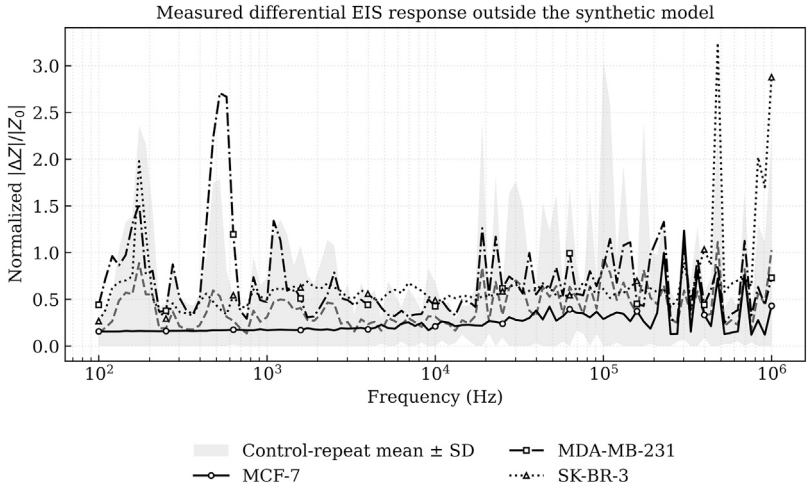

Fig. 10. Independent measured-EIS differential spectra. Mean normalized differential magnitude for MCF-7, MDA-MB-231, and SK-BR-3 cell-associated measurements reconstructed from experimental magnitude and phase data. The gray band denotes the mean ± standard deviation of control–control repeat differences and therefore represents measured repeatability/background variation rather than a clinical negative cohort.

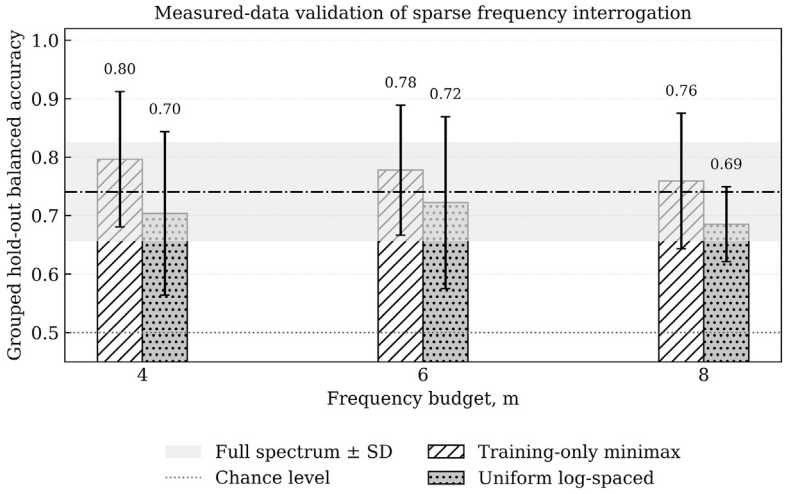

Fig. 11. Measured-data validation of sparse frequency interrogation. Grouped leave-one-sample-out balanced accuracy for training-only empirical minimax frequency selection and log-uniform subsets at budgets $m \in \{4, 6, 8\}$. Bars show mean ± standard deviation across three held-out sample folds. The dash–dot line and gray band show the complete 101-frequency reference, and the dotted line denotes chance-level balanced accuracy.

meaningful because the improvement is consistent across E-optimal, D-optimal, and CRLB-based measures rather than being limited to a single metric.

The first source of improvement is the differential operator. In the paired-channel model, the differential response reduces shared common-mode nuisance under the stated assumptions, which improves the effective quality of the measurement used for estimation. This trend appears clearly in the ablation results, where moving from B1 to B3 improves $\mathcal{M}_E$ and reduces both CRLB proxy metrics (Table 7). In simple terms, the estimator receives cleaner information after subtraction, so the inverse problem becomes better conditioned.

This interpretation is consistent with the Fisher-information formulation. The information matrix depends on both sensitivity and noise covariance, so nuisance cancellation can improve identifiability when useful sensitivity is preserved. The covariance-to-information monotonicity result in the methodology explains why this effect is expected, not accidental.

The second source of improvement is joint co-design. Geometry and frequency choices affect the same Fisher-information matrix, so they should not be optimized independently. The crossover between B5 and B6 shows this clearly: frequency co-design is slightly stronger for some robustness-oriented metrics, while geometry co-design is slightly

stronger for others. This means the two components are complementary, not redundant.

The stronger added frequency-selection baselines also help clarify this point. B7 and B8 improve over the heuristic differential baseline B4 and remain competitive with the partial co-design variants, but they still do not match the full co-design across all reported metrics. This suggests that stronger frequency selection alone is useful, but the largest gain still comes from coupling frequency design with geometry optimization in one minimax formulation.

The full method performs better because it combines these complementary gains. At $m = 6$, it improves $\mathcal{M}_{\mathrm{E}}$ by about 19.3% over B5 and 22.9% over B6, and it reduces $\mathcal{M}_{\mathrm{tr}}$ by about 21.1% and 16.4%, respectively (Table 5). This is the practical value of the joint minimax formulation: it improves the weakest directions of identifiability while preserving strong overall information.

The frequency-budget results also support this view. The proposed method remains best across all tested budgets and is especially strong in the low-budget regime, where measurement efficiency matters most. At $m = 4$, it already reaches high identifiability values compared with the baselines (Table 6). This suggests that the co-design framework does not only improve performance at fixed budget, but also helps reduce the number of interrogated frequencies needed to reach a target performance level.

The robustness results under nuisance and tolerance amplification are also aligned with the design objective. All methods degrade as uncertainty increases, which is expected. However, the proposed method keeps the best absolute performance across the full amplification sweep (Table 8), and the retention summaries show a slower loss of performance in the aggregate figures. This is consistent with a design that was optimized for worst-case behavior rather than nominal conditions only.

The reference-mismatch analysis provides a useful realism check. As mismatch increases, all differential methods degrade because common-mode cancellation becomes less effective. Even so, the proposed method keeps the best absolute values across the tested mismatch levels (Table 9). At the highest mismatch level, retention becomes closer among the strongest differential variants, which suggests that part of the advantage comes from a stronger baseline design before mismatch is introduced. At the same time, these results should not be read as evidence of perfect cancellation in fabricated devices, because additional channel asymmetry and unmodeled parasitic imbalance may further reduce practical differential suppression.

The computational-cost analysis shows a reasonable trade-off for the intended use case. The proposed method is more expensive than heuristic and partial co-design baselines because it jointly updates geometry and frequency variables and refines adversarial scenarios. However, this cost occurs during offline design, not during sensing deployment. For that reason, the runtime increase is acceptable if the goal is a better sensor–protocol design. This interpretation should still be limited to the present in silico setup, since higher-fidelity 3D geometries, denser discretizations, and tighter hardware-aware constraints would increase both runtime and memory demand.

The main geometry–frequency co-design comparison still uses the same synthetic modeling family for optimization and testing. The independent measured-data experiment partially addresses this limitation by showing that a differential empirical minimax strategy can identify informative sparse frequency subsets in out-of-family spectra. However, the selection criterion was re-estimated within each measured-data training fold; the experiment therefore supports transfer of the design principle rather than unchanged transfer of the synthetic optimum (d^*, F^*). The small number of grouped folds and substantial variability also prevent claims of statistical superiority.

For the intended urine-sensing context, the implication remains methodological rather than clinical. The measured-data analysis strengthens the evidence for the differential sparse-frequency component, whereas fabrication of the optimized spiral geometry, direct characterization of channel matching and drift, and testing in urine matrices remain necessary before practical or clinical claims can be made.

8. Limitations and future work

The principal limitation is that the optimized geometry and its joint interaction with the frequency set are still evaluated within the synthetic model family used for design. The independent measured-data experiment reduces the circularity concern for the differential sparse-frequency component, but it uses breast-cancer cell suspensions, nanoprobes, and a different electrode platform. It therefore does not validate the proposed spiral geometry, urine sensing, or bladder-cancer performance. The external dataset is also small, and its control-repeat differences are a repeatability reference rather than a clinical negative cohort.

Practical performance also depends on matching between sensing and reference channels. The synthetic mismatch study shows graceful degradation, but fabricated devices may exhibit additional asymmetry, calibration error, drift, and parasitic imbalance. The framework also has higher offline computational cost than heuristic or partial-design baselines, which may increase with higher-fidelity geometries and denser design spaces.

Future work should therefore fabricate the optimized geometry, measure device-to-device and channel-to-channel variability, and evaluate the design in controlled urine matrices before moving to clinical samples. Larger independent EIS datasets, preregistered frequency sets, and out-of-family hardware measurements are needed to test whether the synthetic optimum transfers unchanged. Faster surrogates and hardware-aware constraints may also reduce offline cost and improve deployability.

9. Conclusion

This study presented a robust in silico co-design framework that combines differential spiral EIS sensing with joint geometry and frequency selection. A minimax Fisher-information objective improved worst-case identifiability and CRLB proxy metrics over single-channel, heuristic, stronger greedy-frequency, and partial co-design baselines at matched frequency budgets. The gains remained visible under frequency-budget variation, amplified nuisance and fabrication tolerances, and reference mismatch.

An independent measured-EIS analysis provided additional component-level evidence outside the synthetic model family. With four selected frequencies, training-only empirical minimax selection achieved 79.6% ± 11.6% balanced accuracy, compared with 70.4% ± 14.0% for log-uniform selection and 74.1% ± 8.5% for the complete 101-frequency spectrum. These findings support the differential sparse-frequency design principle, but they do not validate the optimized spiral geometry or establish urine-, bladder-cancer-, sensor-level, or clinical performance.

Overall, the framework provides a principled basis for robust EIS sensor–protocol design. Fabricated-sensor testing, direct measurement of channel mismatch and drift, and validation in urine matrices are the next required steps toward practical translation.

CRediT authorship contribution statement

Mohanad A. Deif: Writing – review & editing, Writing – original draft, Software, Methodology, Formal analysis, Conceptualization. **Ismail A. Elhaty:** Visualization, Software, Methodology, Investigation, Formal analysis. **Mohamed A. Hafez:** Writing – review & editing, Writing – original draft, Resources, Project administration, Investigation, Funding acquisition, Formal analysis. **Mohammad Khishe:** Writing – review & editing, Writing – original draft, Supervision, Software, Methodology, Investigation, Formal analysis.

Code availability

The measured-data preprocessing script is provided as Supplementary Code S1 (`Supplementary_Code_S1_Prepare_Measured_EIS_Dataset.py`), and the complete independent measured-data validation workflow is provided as Supplementary Code S2 (`Supplementary_Code_S2_Measured_EIS_Validation.py`). The validation script reproduces the reported frequency selections, fold-level metrics, summary statistics, and figures from Supplementary Data S1. Code used for the synthetic forward model, optimization, and geometry–frequency co-design experiments is available from the corresponding author upon reasonable request.

Ethics approval and consent to participate

This study comprised synthetic computational experiments and secondary analysis of publicly available, previously published impedance measurements from established cell lines. No new human participants, human specimens, or animals were recruited, collected, or experimentally investigated; therefore, additional ethics approval and informed consent were not required.

Funding

The authors received no specific funding for this work.

Declaration of competing interest

The authors declare that they have no conflict of interest relevant to the content of this work.

Data availability

Processed EIS data and validation code are provided as supplementary files. Original data are publicly available from Huerta-Nuñez et al. (2019), http://dx.doi.org/10.1038/s41598-019-42776-9.

References

[1] E. Barsoukov, J.R. Macdonald (Eds.), Impedance Spectroscopy: Theory, Experiment, and Applications, second ed., John Wiley & Sons, 2005.
[2] A. Lasia, Electrochemical Impedance Spectroscopy and Its Applications, Springer, New York, 2014, http://dx.doi.org/10.1007/978-1-4614-8933-7.
[3] S. Wang, J. Zhang, O. Gharbi, V. Vivier, M. Gao, M.E. Orazem, Electrochemical impedance spectroscopy, Nat. Rev. Methods Prim. 1 (2021) 41, http://dx.doi.org/10.1038/s43586-021-00039-w.
[4] A.C. Lazanas, M.I. Prodromidis, D.D. Karnaushenko, D.D. Karnaushenko, A. Münchinger, O.G. Schmidt, Electrochemical impedance spectroscopy: A tutorial, ACS Meas. Sci. Au 3 (4) (2023) 162–193, http://dx.doi.org/10.1021/acsmeasuresciau.2c00070.
[5] H.S. Magar, R.Y.A. Hassan, A. Mulchandani, Electrochemical impedance spectroscopy (EIS): Principles, construction, and biosensing applications, Sensors 21 (19) (2021) 6578, http://dx.doi.org/10.3390/s21196578.
[6] J.S. Daniels, N. Pourmand, Label-free impedance biosensors: Opportunities and challenges, Electroanalysis 19 (12) (2007) 1239–1257, http://dx.doi.org/10.1002/elan.200603855.
[7] E. Katz, I. Willner, Probing biomolecular interactions at conductive and semiconductive surfaces by impedance spectroscopy: Routes to impedimetric immunosensors, DNA-sensors, and enzyme biosensors, Electroanalysis 15 (11) (2003) 913–947, http://dx.doi.org/10.1002/elan.200390114.
[8] European Association of Urology, Non-muscle-invasive bladder cancer, 2025, EAU Guidelines webpage (2025 limited update noted on page); (Accessed 22 February 2026), https://uroweb.org/guidelines/non-muscle-invasive-bladder-cancer.
[9] American Urological Association, Bladder cancer: Non-muscle invasive guideline, 2024, AUA Guideline webpage; (Accessed 22 February 2026), https://www.auanet.org/guidelines-and-quality/guidelines/bladder-cancer-non-muscle-invasive-guideline.
[10] M.I. Prodromidis, Impedimetric immunosensors—A review, Electrochim. Acta 55 (14) (2010) 4227–4233, http://dx.doi.org/10.1016/j.electacta.2009.01.081.
[11] R. Kumar, R.K. Ratnesh, R.K. Chauhan, A. Kumar, M.K. Singla, R. Gupta, Non-invasive bio-impedance imaging and sensing for medical diagnostics and industrial applications, Journal of The Electrochemical Society 171 (10) (2024) 107510, http://dx.doi.org/10.1149/1945-7111/ad830b.
[12] X. Jiang, et al., A finite element approach for optimizing interdigitated electrode design to enhance sensitivity in impedance biosensors, Results Eng. 23 (2024) 102549, http://dx.doi.org/10.1016/j.rineng.2024.102549.
[13] J. Ojarand, M. Min, A. Koel, Multichannel electrical impedance spectroscopy analyzer with microfluidic sensors, Sensors 19 (8) (2019) 1891, http://dx.doi.org/10.3390/s19081891.
[14] S. Neshani, et al., AC and DC differential bridge structure suitable for electrochemical interfacial capacitance biosensing applications, Biosensors 10 (3) (2020) 28, http://dx.doi.org/10.3390/bios10030028.
[15] S. Neshani, et al., A differential capacitance readout interface with common-mode-to-differential conversion for biosensors, Sensors 23 (20) (2023) 8581, http://dx.doi.org/10.3390/s23208581.
[16] Z. Javaid, M.A. Iqbal, S. Javeed, S.S. Maidin, K. Morsy, A.A. Shati, J.R. Choi, Reviewing advances in nanophotonic biosensors, Front. Chem. 12 (2024) 1449161, http://dx.doi.org/10.3389/fchem.2024.1449161.
[17] A. Kandwal, S. Dutt, L.W.Y. Liu, Z. Nie, R. Jasrotia, C.K. Chan, A.M. Almuhlafi, H. Vettikalladi, Frequency selective metasurface based radio frequency glucose sensor with a periodic array of meta cells, Sci. Rep. 14 (2024) 25716, http://dx.doi.org/10.1038/s41598-024-76741-y.
[18] S.M. Kay, Fundamentals of Statistical Signal Processing, Volume I: Estimation Theory, Prentice Hall, Upper Saddle River, NJ, 1993.
[19] F. Pukelsheim, Optimal Design of Experiments, SIAM, Philadelphia, 2006, http://dx.doi.org/10.1137/1.9780898719109.
[20] A.C. Atkinson, A.N. Donev, R.D. Tobias, Optimum Experimental Designs, with SAS, Oxford University Press, Oxford, 2007.
[21] X. Huan, J. Jagalur, Y. Marzouk, Optimal experimental design: Formulations and computations, Acta Numer. 33 (2024) http://dx.doi.org/10.1017/S0962492924000023.
[22] C.R. Rojas, J.S. Welsh, G.C. Goodwin, A. Feuer, Robust optimal experiment design for system identification, Automatica 43 (6) (2007) 993–1008, http://dx.doi.org/10.1016/j.automatica.2006.12.013.
[23] T.S. Aghdam, S.M.M. Alavi, M. Saif, Structural identifiability of impedance spectroscopy fractional-order equivalent circuit models with two constant phase elements, Automatica 144 (2022) 110463, http://dx.doi.org/10.1016/j.automatica.2022.110463.
[24] V.V. Fedorov, S.L. Leonov, Optimal Design for Nonlinear Response Models, CRC Press, Boca Raton, 2014, http://dx.doi.org/10.1201/b17470.
[25] L. Ljung, System Identification: Theory for the User, second ed., Prentice Hall, Upper Saddle River, NJ, 1999.
[26] É. Walter, L. Pronzato, Identification of Parametric Models from Experimental Data, first ed., Springer, London, 1997.
[27] J. Wekalao, H.A. Elsayed, O. El Amri, S. Mostafa, A. Mehaney, Design and optimization of a graphene-enhanced terahertz metasurfaces surface plasmon resonance biosensor with multi-material architecture for cancer detection integrating 1D-CNN machine learning for performance prediction and analysis, Plasmonics (2025) http://dx.doi.org/10.1007/s11468-025-02912-w.
[28] A. Mehaney, A.M. El-Sherbeeny, J. Wekalao, Machine learning-enhanced surface plasmon resonance biosensor with multilayer BK7/ag/WS_2/graphene architecture for ultrasensitive tuberculosis biomarker detection, Microchem. J. 218 (2025) 115397, http://dx.doi.org/10.1016/j.microc.2025.115397.
[29] L.F.E. Huerta-Nuñez, G. Gutierrez-Iglesias, A. Martinez-Cuazitl, M.M. Mata-Miranda, V.D. Alvarez-Jiménez, V. Sánchez-Monroy, A. Golberg, C.A. González-Díaz, A biosensor capable of identifying low quantities of breast cancer cells by electrical impedance spectroscopy, Sci. Rep. 9 (2019) 6419, http://dx.doi.org/10.1038/s41598-019-42776-9.